applied sciences

Article

Spatial Characterization of Single-Cracked Space Based on Microcrack Distribution in Sandstone Failure

Xiaolin Hou [1,2,3,*], Hongyu Zhai [1], Chunlai Wang [2], Tingting Wang [1], Xiang He [4], Xiang Sun [5,6], Zhian Bai [2], Baokun Zhou [2] and Xiaoshuang Li [7]

1 Institute of Geophysics, China Earthquake Administration, Beijing 100081, China
2 School of Energy and Mining, China University of Mining and Technology Beijing, Beijing 100083, China
3 Norman B. Keevil Institute of Mining Engineering, University of British Columbia, Vancouver, BC V6T 1Z4, Canada
4 School of Mining Engineering, Anhui University of Science and Technology, Huainan 232001, China
5 School of Civil Engineering and Architecture, Wuyi University, Wuyi 354300, China
6 Engineering Research Center of Prevention and Control of Geological Disasters in Northern Fujian, Fujian Province University, Wuyi 354300, China
7 School of Civil Engineering, Shaoxing University, Shaoxing 312000, China
* Correspondence: houxl@cea-igp.ac.cn; Tel.: +86-010-6872-9009

Abstract: To further understand the rock damage zone, an approach based on microcrack distribution was proposed to characterize the crack space of rock specimens in this research. Acoustic emission (AE) technology was utilized on sandstone to obtain the spatial distribution of microcracks in which uniaxial compression forms the single-cracked fracture. The proposed theoretical distribution pattern space (TDPS), 3D convex hull, and the minimum volume enclosing ellipsoid (MVEE) algorithms were adopted to analyze the geometric features of the crack space. It was found that the 3D convex hull method returned the smallest results in both area and volume of the crack space, and the largest results were provided by the proposed TDPS method. The difference between the results of the proposed TDPS method and the MVEE method became smaller after 85%. The deviation angle of the principal axis of the cracked space gradually decreased as the spatial scale decreased, while the other two major axes exhibited a tendency to increase at the 65% scale. The results indicate that a spatial scale from 65% to 85% is a reliable range for the characterization of crack space.

Keywords: crack space; acoustic emission; TDPS method; MVEE method; 3D convex hull method

check for updates

Citation: Hou, X.; Zhai, H.; Wang, C.; Wang, T.; He, X.; Sun, X.; Bai, Z.; Zhou, B.; Li, X. Spatial Characterization of Single-Cracked Space Based on Microcrack Distribution in Sandstone Failure. *Appl. Sci.* **2023**, *13*, 1462. https://doi.org/10.3390/app13031462

Academic Editors: Ricardo Castedo and Tiago Miranda

Received: 6 December 2022
Revised: 31 December 2022
Accepted: 17 January 2023
Published: 22 January 2023

1. Introduction

Crack distribution in rock fracture is crucial for finding and understanding the damage zone, which can be used to indicate the extent and the potential direction of crack propagation [1,2]. Therefore, the distribution characterization of the cracks plays a fundamental role in the damage assessment of rock compression failure.

The distribution of the cracks in rocks has been realized from different spatial dimensions, such as the 2D crack space assessment of cracks on the rock surface, including digital image correlation technology [3], infrared thermal imaging technology [4], optical observation technology [5], etc. There are methods for 3D crack space assessment of cracks inside the rock, including computer tomography [6], acoustic emission (AE) [7], etc. They demonstrated the power of acquiring crack distribution from light waves, electromagnetic waves, and sound waves. It is known that the original openings inside the rock are dislocated under loading, and the released energy during rupture propagates through the rock in the form of elastic waves, monitored as AE [8]. It has been widely used in rock mechanics and engineering for damage assessment and hazard warning [9–11].

AE monitoring was performed on rock failure experiments with different loading methods and paths, and the microcrack distribution results successfully indicated the real rupture location and the coincident damage shape [12–18]. As a result, the microcracks were found to be more prevalent in severely damaged zones in the laboratory and the field [9]. Therefore, for a better visualization of the damage zone directly by the microcrack, the density estimation method was adopted on the microcrack distribution results to find severely damaged areas [19,20]. Furthermore, the micro-seismic events detected in earthquakes were displayed within a 2D map from different cross-sectional views [21]. The mainshocks could be found by the density contour [22]. The results from the high-density area demonstrate that microcracks have a potential elliptical distribution pattern [20]. Moreover, ellipsoidal-like results were observed in a granite boulder by a 3D kernel density estimation [23]. These studies provide strong evidence for the hypothesis theory that the single-cracked space is of ellipsoidal distribution, and demonstrate the feasibility of single-cracked space in characterizing rock failure studies.

In addition, it is worth noting that crack recognition of multiple cracks was performed in the triaxial compression experiments, and the results of crack space characterized by ellipsoids were consistent with macrocrack rupture surfaces, and the distribution pattern has been proven [24,25]. However, further investigation of the relationship between crack space and mechanics, and the optimization on the crack space size needs to be implemented for a more accurate result.

The investigations of the spatial distribution of cracks have focused on hydraulic fracturing. In particular, the stimulated reservoir volume (SRV) was proposed to estimate the storage of oil and gas [26–28]. Convex optimization algorithms such as 3D convex hull and minimum volume enclosing ellipsoid (MVEE) were successfully adopted to evaluate the SRV from the perspective of microcracks [29–31].

However, the mechanism and mechanical behavior are different between hydraulic fracturing and compression failure in rocks. First, the fracturing fluid acts as a stressor in the process of hydraulic fracturing, accompanied by physical and chemical reactions. The fluid flows in via the hydraulic crack and forms a tensile stress zone near the non-closed fracture zone, resulting in the continuous expansion of the fracture and the eventual formation of the stimulated reservoir volume [32]. In contrast to hydraulic fracturing, the role of fluids is missing in regular rock compression failure. In the second, the mechanisms of rock compression failure include not only tensile failure, but also a part of shear failure [33–36]. Through RA-AF and moment tensor, both mechanisms have been identified in the rupture of rock compression tests and tensile tests [16,37]. More importantly, the objective of SRV estimation is to seek volume size rather than the spatial distribution pattern of microcracks under loading conditions. Despite the differences between hydraulic fracturing and rock compression fractures, they share similarities of microcracks distributed in an ellipsoid pattern [23,27,28,38]. Therefore, the methods of SRV assessment can be applied to evaluate the crack space of the compression failure test. Furthermore, the relationship between crack space deformation and load needs to be considered in addition to the volume of the crack space.

In this paper, AE monitoring was performed on sandstone specimens, which was used to obtain the microcracks of single-cracked fracture in uniaxial compression experiments. The theoretical distribution pattern space (TDPS) model was established based on the 3D spatial deformation. The MVEE algorithm and the 3D convex hull algorithm were adopted to approach the minimum crack space from different perspectives. As the scale of the crack space varies, the geometric features and evolutionary patterns of crack space were investigated by the three optimization methods. The proposed crack space model can be used to analyze the rock damage subject to compression failure and provide a reference for assessing rock damage with microcracks.

2. Materials and Experimental Procedure

The rock samples used in this research were drilled from the No. 5 coal seam floor of a mine in Lvliang, Shanxi Province, China, and they are sandstone. The sampled seam is in the lower to middle part of the Shanxi Formation. The Shanxi Formation is an interlocking sea–land coal-bearing deposit with an average thickness of 57.38 m, consisting mainly of sandy mudstone, carbonaceous mudstone, fine sandstone, and coal seams, where the sandstone is of medium-grain structure, laminated, and mud-cemented.

In addition, the rock samples were selected for the absence of visible joints, ensuring that complex multi-crack failure would hardly occur after the uniaxial compression testing. Seven specimens were polished into cylinders with a diameter of 70 mm and a height of 140 mm, as shown in Figure 1a. The average density of the specimens was 2.39 g/cm^3 with a uniaxial compressive strength of 51.21 $\pm$ 4.01 MPa. Two specimens were used for pre-experiment testing and scanning electron microscopy (SEM) testing, and five specimens were adopted for single-cracked testing.

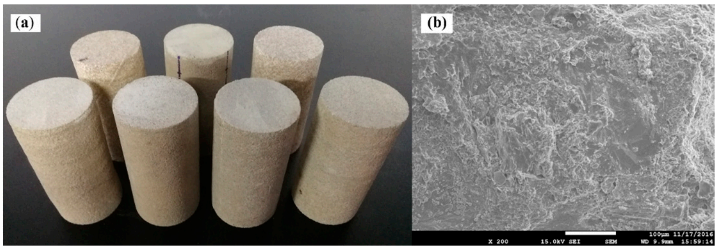

Figure 1. Sandstone specimens and fracture surface SEM. (**a**) Raw rock samples; (**b**) SEM of specimen at 200x magnification.

The SEM analysis result shows that at the micrometer scale, the cross-section is irregular, there are debris and a few original voids, the sedimentary distribution is disorganized, and the microstructure is not sufficiently cemented, as shown in Figure 1b. The results indicate that the sandstone particles are loosely cemented, and the microstructure is complex, reflecting the inhomogeneity of the sandstone and providing an interpretation for the generation of sub-cracks from sandstone damage.

The single-cracked test was performed in a rock mechanics test system. It provides a loading speed in the range of 0.01 kN/s to 20 kN/s. The spatial distribution of microcracks was obtained by the acoustic emission monitoring system. The AE monitoring system consists of the AE processing system PCI-Express 8 model from Physical Acoustic Corporation, 5 AE sensors in the Nano 30 model, preamplifiers in the 1220A-AST model, and connection cables. The Nano 30 model has a resonant frequency of 140 kHz and an operating frequency from 150 to 400 kHz, which is in line with the expected frequency range for rock failure monitoring. A schematic of the mechanical loading and AE monitoring is shown in Figure 2a. The layout of the AE sensors is shown in Figure 2b.

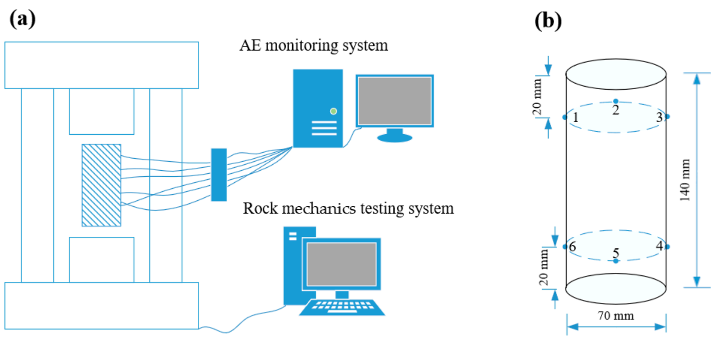

Figure 2. A schematic diagram of the uniaxial loading and AE monitoring system. (**a**) The schematic diagram of the uniaxial loading; (**b**) the schematic diagram of an AE sensor's layout.

The loading test was implemented by uniaxial loading controlled by displacement, and the loading speed was set at 0.1 mm/min. Based on previous experimental experience and lead break tests [9,24,25], in this AE monitoring test, the acquisition threshold was set to 45 dB for minimizing the environmental noise effect, the sampling frequency was set to 1 MHz, and the preamplifier gain was set to 40 dB.

3. Spatial Characterization Methods

3.1. 3D Convex Hull Algorithm

Consider a subset S contains n points, where the line segment connecting any two points is contained. The convex hull is defined as the smallest convex set. To find the smallest convex hull in 3D, an initial hull with four facets is formed. Before new points are added to the hull gradually to form a new hull, the point farthest away from the facet should be added to the hull first. Points inside the hull are ignored and added to a visible set V. For the point outside the hull, the unassigned point that above the facet is added to an outside set FO. Then, calculate the point in the outside set FO, and put visible points into set V, ensuring that no other points are visible in the outside set. The boundary of V is the set of horizon ridges. Then, a new facet is created from each ridge and point p. The new hull is formed after deleting the old facets in V.

In this research, the quickhull algorithm was used to find the convex hull [39]. Delaunay triangulation was the method used to implement the triangulation function.

3.2. Minimum Volume Enclosing Ellipsoid Algorithm

Compared with the 3D convex hull, the ellipsoid is more prominent in spatial characteristics. It has clear three-axis distribution characteristics, which can be used to calculate geometric characteristics such as crack direction and crack surface. The equation of the ellipsoidal surface is given as:

$$ax^2 + by^2 + cz^2 + 2dxy + 2exz + 2fyz + 2gx + 2hy + 2iz = 1 \tag{1}$$

Nine parameters from a to i can be solved with more than 9 points [29]. However, an ellipsoidal surface may not be formed when solving the surface equation, due to the irregular distribution of scattered points. In the field of convex optimization, the MVEE can be used to solve this obstacle [40].

Consider a set of $\boldsymbol{m}$ points in $\boldsymbol{n}$ dimensional crack space $\boldsymbol{R}^n$: $\boldsymbol{S} = \{s_1, s_2, \cdots s_m\} \in \boldsymbol{R}^n$. To guarantee that the ellipsoid has positive volume in any condition, it is assumed that the convex hull of the set $\boldsymbol{S}$ spans $\boldsymbol{R}^n$. Therefore, the ellipsoid ε in center form is given by:

$$\varepsilon = \left\{ \boldsymbol{s} \in \boldsymbol{R}^n \middle| (\boldsymbol{s} - \boldsymbol{c})^T \boldsymbol{E}_m (\boldsymbol{s} - \boldsymbol{c}) \leq 1 \right\} \tag{2}$$

where $\boldsymbol{c}$ is the center of the ellipsoid, $\boldsymbol{E}_m \in \boldsymbol{S}^n_{++}$, and $\boldsymbol{E}_m$ is a positive definite matrix. Thus, the volume of ellipsoid ε is given by:

$$V(\varepsilon) = \frac{v_0}{\sqrt{\det(\boldsymbol{E}_m)}} \tag{3}$$

where v_0 is the volume of the unit hypersphere. Therefore, this problem is equivalent to finding a vector $\boldsymbol{c}$ and a positive definite matrix $\boldsymbol{E}_m$, which minimizes $\det(\boldsymbol{E}_m)$.

Optimizing the problem into a convex optimization problem, the problem can be solved easier in the following dual problem:

$$\begin{cases} \max \log \det V(\boldsymbol{u}) \\ \text{subject to } \boldsymbol{1}^T \boldsymbol{u} = 1 \end{cases} \tag{4}$$

where $\boldsymbol{V}(u) = \boldsymbol{Q}\mathrm{dig}(\boldsymbol{u})\boldsymbol{Q}^T$, $\boldsymbol{Q} = \begin{bmatrix} \boldsymbol{P} & \boldsymbol{1}^T \end{bmatrix}^T \in \boldsymbol{R}^{(n+1)\times m}$, $\boldsymbol{P} = [p_1, p_2, \cdots p_m] \in \boldsymbol{R}^{n\times m}$ and $\boldsymbol{u} = [u_1, u_2, \cdots u_m]^T$, $u_i \geq 0$.

An ascent method is adopted to find the maximum. The ascent direction at a feasible point $\overline{\boldsymbol{u}}$ is $\Delta u = \boldsymbol{e}_j - \overline{\boldsymbol{u}}$, where $j = \underset{i}{\operatorname{argmax}} g_i(\overline{\boldsymbol{u}})$ in the j-th unit vector $\boldsymbol{e}_j$, and $g_i(\boldsymbol{u}) = \boldsymbol{q}_i{}^T \boldsymbol{V}(u)^{-\mathbf{1}} \boldsymbol{q}_i$. The problem can be approached [41] with

$$\max_{\alpha \in [0,1]} \log \det V\left(\overline{\boldsymbol{u}} + \alpha\left(\boldsymbol{e}_j - \overline{\boldsymbol{u}}\right)\right) \tag{5}$$

where the α is

$$\alpha = \frac{g_i(\overline{\boldsymbol{u}}) - (n+1)}{(n+1)(g_i(\overline{\boldsymbol{u}}) - 1)} \tag{6}$$

3.3. Theoretical Distribution Pattern Space

With the rock specimen in mechanical equilibrium, we assume that a virtual unit crack space exists in the n dimension in the form of a sphere space, which also remains in equilibrium in all directions. Therefore, it can be represented by Equation (7) as

$$\|\boldsymbol{r}\|^2 = r_1{}^2 + r_2{}^2 + \cdots + r_n{}^2 = 1 \tag{7}$$

where the vector $\boldsymbol{r}$ has a length of 1 in all directions. Deformation occurs when the unit crack space is exposed to an applied stress σ. In general, the stress σ can be decomposed into n components in different directions, such as σ_1, σ_2, $\cdots$, σ_n, and the orientations of the components are $a_1, a_2, \cdots, a_n$, respectively. When the crack space is balanced, the stress conditions in the deformed crack space can be written as follows:

$$\frac{r_1{}^2}{|\sigma_1|^2} + \frac{r_2{}^2}{|\sigma_2|^2} + \cdots + \frac{r_n{}^2}{|\sigma_n|^2} = 1 \tag{8}$$

When the stress values in all orientations are equal, the crack space still maintains a sphere. In 3D space, the crack space is thereby assumed to have three orientations perpendicular to each other.

As we know, the internal defects are misaligned when the materials are subjected to stress, causing microcracks, and they are detected by AE monitoring. Moreover, it was found that the crack propagation surface produced is perpendicular to the minor principal stress direction [28,32]. Since the three decomposed stress orientations are perpendicular to each other, the microcracks should propagate along the other two stress orientations. Therefore, microcracks are assumed to be distributed along the stress orientations. It can be inferred that the orientations of the microcrack distribution (theoretically, crack space), the stress, and the real crack should be consistent. Therefore, the distribution characteristics of the microcracks can theoretically be used to characterize either the stress or the real crack.

At the same time, the scale of microcrack propagation varies in all directions due to the different values of stress components. Assuming a linear relationship between the stress value and the length of microcrack propagation, the theoretical distribution pattern space can be established as

$$\frac{x^2}{a^2} + \frac{y^2}{b^2} + \frac{z^2}{c^2} = 1 \tag{9}$$

where a, b, and c are the scales of microcrack propagation of the three decomposed stresses σ_a, σ_b, and σ_c, respectively.

On the basis of the above theoretical analysis, the optimal three directions for characterizing the spatial distribution of microcracks $\boldsymbol{S}(\boldsymbol{x}, \boldsymbol{y}, \boldsymbol{z})$ can be found. Mathematically, the variance $\mathrm{Var}(\boldsymbol{S}^*)$ of the projection of microcracks in the target direction should be the largest. Second, every two directions need to be perpendicular to each other to avoid correlation. The covariance $\mathrm{Cov}\left(\boldsymbol{s}_i{}^*, \boldsymbol{s}_j{}^*\right)$ between the projected data in each of the two directions should be zero. The variance and the covariance are in the form:

$$\mathrm{Var}(\boldsymbol{s}^*) = \frac{1}{m} \sum_{i=1}^{m} \left(\boldsymbol{s}_i{}^* - \overline{\boldsymbol{s}^*}\right)^2 = \frac{1}{m} \sum_{i=1}^{m} \boldsymbol{s}_i{}^{*2} \tag{10}$$

$$\mathrm{Cov}\left(\boldsymbol{s}_i{}^*, \boldsymbol{s}_j{}^*\right) = \frac{1}{m}\sum_{i=1}^{m} \boldsymbol{s}_i{}^* \boldsymbol{s}_j{}^* \tag{11}$$

It is found that two conditions can be satisfied by diagonalizing the covariance matrix $\boldsymbol{C}_{S^*}$:

$$\boldsymbol{C}_{S^*} = \frac{1}{m}\boldsymbol{S}^*\boldsymbol{S}^{*T}\begin{pmatrix} \frac{1}{m}\sum\limits_{i=1}^{m} \boldsymbol{x}_i{}^{*2} & \frac{1}{m}\sum\limits_{i=1}^{m} \boldsymbol{x}_i{}^*\boldsymbol{y}_i{}^* & \frac{1}{m}\sum\limits_{i=1}^{m} \boldsymbol{x}_i{}^*\boldsymbol{z}_i{}^* \\ \frac{1}{m}\sum\limits_{i=1}^{m} \boldsymbol{x}_i{}^*\boldsymbol{y}_i{}^* & \frac{1}{m}\sum\limits_{i=1}^{m} \boldsymbol{y}_i{}^{*2} & \frac{1}{m}\sum\limits_{i=1}^{m} \boldsymbol{y}_i{}^*\boldsymbol{z}_i{}^* \\ \frac{1}{m}\sum\limits_{i=1}^{m} \boldsymbol{x}_i{}^*\boldsymbol{z}_i{}^* & \frac{1}{m}\sum\limits_{i=1}^{m} \boldsymbol{y}_i{}^*\boldsymbol{z}_i{}^* & \frac{1}{m}\sum\limits_{i=1}^{m} \boldsymbol{z}_i{}^{*2} \end{pmatrix} \tag{12}$$

where the variances are on the diagonal of the matrix $\boldsymbol{C}_{S^*}$, and the other elements are covariances, as shown in Equation (12). The covariance matrices $\boldsymbol{C}_{S^*}$ and $\boldsymbol{C}_S$ have a relationship as follows:

$$\boldsymbol{C}_{S^*} = \frac{1}{m}\boldsymbol{S}^*\boldsymbol{S}^{*T} = \frac{1}{m}(\boldsymbol{WS})(\boldsymbol{WS})^T = \boldsymbol{WC}_S\boldsymbol{W}^T \tag{13}$$

Therefore, $\boldsymbol{C}_{S^*}$ can be obtained when the matrix $\boldsymbol{W}$ satisfies the matrix $\boldsymbol{WC}_S\boldsymbol{W}^T$ as a diagonal matrix. Since the covariance matrix $\boldsymbol{C}_S$ is a symmetric matrix, a diagonal matrix $\boldsymbol{\Lambda}$ can be found by

$$\boldsymbol{\Lambda} = \boldsymbol{E}^T\boldsymbol{C}_S\boldsymbol{E} \tag{14}$$

where the $\boldsymbol{E}$ is the matrix consisting of 3 sets of unit orthogonal vectors. $\boldsymbol{E}^T$ is equal to $\boldsymbol{W}$. Therefore, the matrix $\boldsymbol{W}$ can be calculated by solving the eigenvector of the covariance matrix $\boldsymbol{C}_S$. The projected data $\boldsymbol{S}^*$ and its covariance matrix $\boldsymbol{C}_{S^*}$ can then be obtained as well.

Furthermore, the theoretical distribution pattern space can be demonstrated in the matrix with the covariance matrix $\boldsymbol{C}_{S^*}$, where the eigenvalues and eigenvectors can be used to calculate the propagation scales and propagation directions of crack, respectively.

A schematic of the spatial characterization by the three methods is presented in Figure 3. The black dots are the monitored events, the two red ellipsoids are given by the DTPS method at two different scales, the gray ellipsoid is calculated by the MVEE method, and the blue irregular convex body is formed by the 3D Convex Hull method.

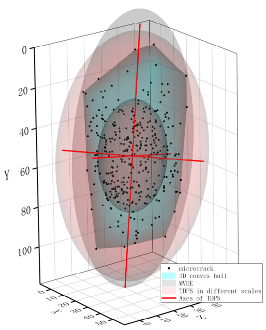

Figure 3. The schematic of three spatial characterization methods. Black dots mark the microcracks, the black ellipsoid represents the space formed by MVEE, the red ellipsoids represent the TDPS space at two different scales, where the three red line segments are the three axes of TDPS, and the cyan irregular geometry is formed by 3D convex hull.

4. Experimental Results

After the sandstone specimens failed, the main cracks were observed to be distributed obliquely and penetrate the specimen, as shown in Figure 4. Part of the material laminated off near the specimen surface. The microcracks obtained in specimen S1 were found to gather at the lower part of the rock specimen. Compared with the size of real cracks through the specimen, there is an error in characterizing the size of the crack space with these microcracks. Therefore, the data of specimen S1 were not adopted. The sandstone specimens after failure and the monitored microcracks are shown in Figure 4. The letters (a), (b), (c), and (d) represent specimens S2, S3, S4, and S5. Letter (e) indicates the stress and event amplitude variation of specimen S3 in time scale.

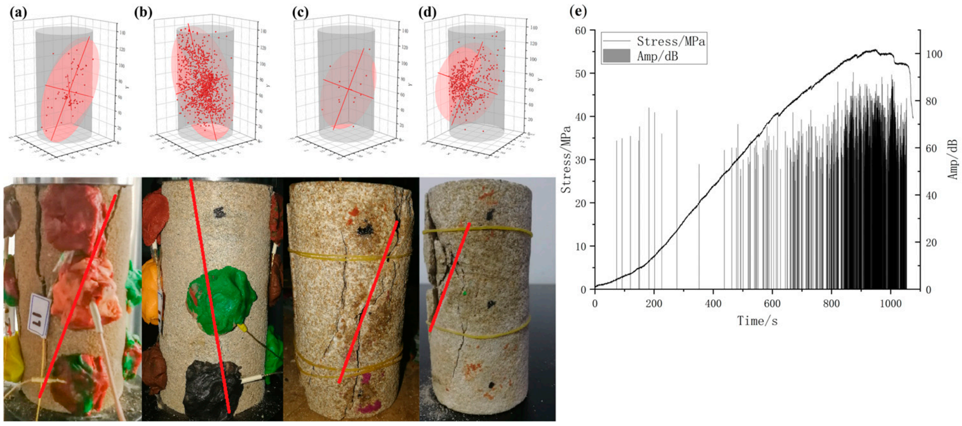

Figure 4. The results of loading and AE monitoring. (**a**) Results for specimen S2 failure and its 71 AE events. (**b**) Results for specimen S3 and its 1069 events. (**c**) Results for specimen S4 and its 14 AE events. (**d**) Results for specimen S5 and its 469 events. (**e**) Variation in stress and event amplitude in specimen S3.

Different numbers of events were obtained under the same equipment and testing settings, with 71, 1069, 14, and 469 events from specimens S2 to S5, respectively. It can be observed that the more severely damaged specimens are, the fewer events monitored. For example, in the experiment, two larger cracks were formed in specimen S2, while a smaller crack was found in specimen S3. The number of events in specimen S2 is less than in specimen S3. In addition, compared with specimen S5, specimen S4 has lower integrity after failure. The number of events in specimen S5 is higher than in specimen S4.

5. Analysis and Discussion

Despite the number of events that vary with the same equipment and settings, the number of parameters AE hit was large for each specimen tested. This result rules out a malfunction of the machine or an error in the parameter settings. In addition to the anisotropy and inhomogeneity of the rock specimens, this result can be explained by the presence of a relatively large crack that hinders the propagation of the microcrack signals from one side to the other [42]. The result coincides with the variability and uncertainty of rock failure monitoring in both the field and in laboratory conditions.

To characterize the crack space, the TDPS method, the MVEE method, and the 3D convex hull method were adopted to evaluate the 3D geometric characteristics of the crack. The 3D convex hull method can obtain a relatively minimum space in three methods. The area and volume of the smallest space can be calculated, but the directional features are difficult to characterize parametrically, especially when the microcracks are not strictly distributed according to a regular geometric distribution pattern. From Section 3.3, the TDPS is assumed to be characterized as an ellipsoid. It is a regular geometric space considering the relationship between stress conditions and microcrack initiation. The geometric directional characteristics are fixed when different crack spatial scales (in percentages) are selected. However, the minimum volume and area are not guaranteed. As a result, it may differ from the results of other optimization methods at the same spatial scale. Fortunately, the MVEE method was proposed to achieve the primary goal of minimum volume while the geometric characteristics can be obtained by solving the MVEE matrix. Therefore, the smallest enclosed space is calculated under this constraint, and displayed as an ellipsoid. However, it is worth noting that the geometric directional characteristics are not guaranteed with different crack spatial ranges.

Therefore, the 3D convex hull method and the MVEE method were adopted to evaluate the theoretical distribution pattern space from the area, volume, and orientation characteristics. Specimens S2, S3, and S5 were selected to represent different orders of magnitude of microcracks. Since the nucleation zone shares similar mechanisms of micro-crack initiation, growth, and coalescence [43–45], different spatial scales of microcracks could be selected to characterize the optimal crack space. In this research, microcracks in each specimen were selected for analysis ranging from 50% to 100% of the theoretical distribution pattern space, and the interval of variation is 5%. Figure 5 shows the results of three spatial characterization methods for 11 stages in specimen S3.

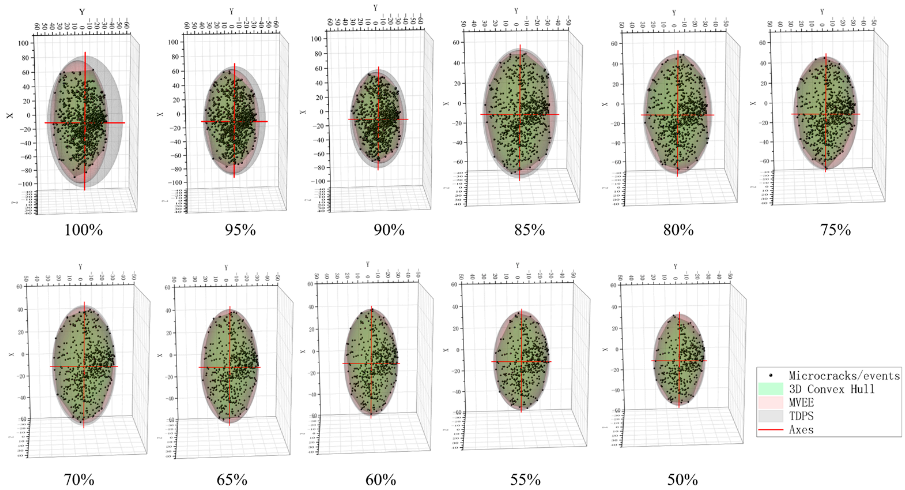

Figure 5. The spatial characterization results of specimen S3. Black dots mark the microcracks, the red ellipsoid represents the space formed by MVEE, the black ellipsoid represents the TDPS space, where the three red line segments are the three axes of TDPS, and the yellow irregular geometry is formed by 3D convex hull.

5.1. Area and Volume Evaluation at Different Spatial Scales

As shown in Figure 6, the evaluations of the area at different spatial scales were obtained. Figure 6a–c presents the area evolution results of specimens S2, S3, and S5, respectively.

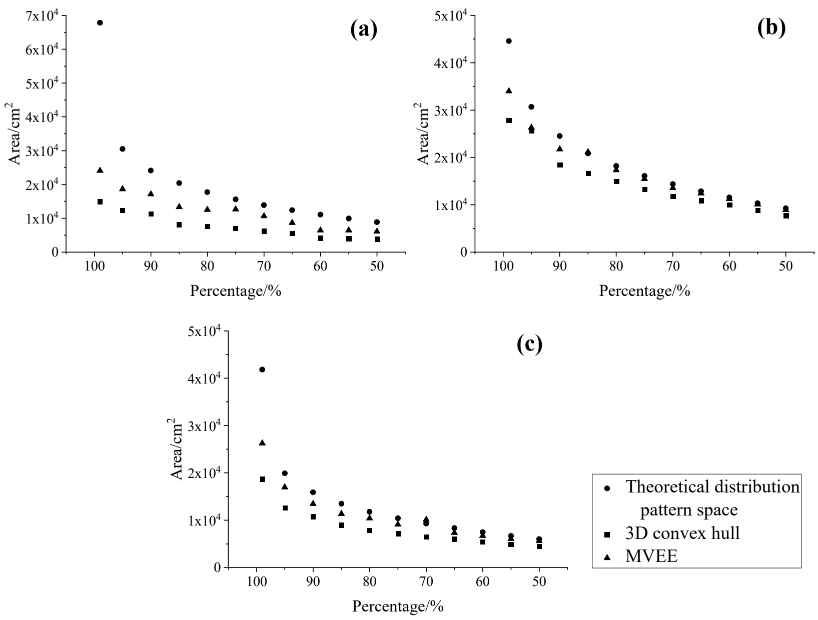

Figure 6. Area evaluation of three methods. (**a**) Area evaluation of Specimen S2. (**b**) Area evaluation of Specimen S3. (**c**) Area evaluation of Specimen S5.

In Figure 6a, the theoretical result at the 100% position is relatively large. The rest of the values show potential regularity. It is possible that the number of microcracks monitored in this specimen is relatively small and the distribution is sparse. Therefore, the variation is significantly on a larger base when the range of spatial scales is reduced. It can also be interpreted as a similar variation at 100% for the other two specimens, as shown in Figure 6b,c. However, due to a greater number of microcracks, the density of microcracks in the other two specimens is relatively greater. Therefore, the differences were lower compared to specimen S2, and even a similar fall was found in specimens S3 and S5.

Among the three methods, it is found that the area evaluation results from the theoretical distribution pattern space are the largest, and the 3D convex hull result has the smallest values. As the scale of selected intervals decreases, the values of the three methods gradually become closer. In general, the values in the MVEE method are closer to the TDPS method results than the 3D convex hull results. It is possible that both the TDPS method and the MVEE method are based on an ellipsoid space, which can degenerate into a sphere space, the area values are closer, and the MVEE results are lower than those of the theoretical distribution pattern space because of the minimum volume target. Therefore, this relationship can be used to find the optimal characterization interval of the theoretical distribution pattern space.

In spite of the differences in microcrack density and the area variation from the results of three specimens, the values of the TDPS and MVEE method are closer to each other in the interval below 85%. The position is illustrated by the distance between the circle and triangle symbols in the figure.

As shown in Figure 7, the volume evaluation results at different spatial scales in three methods were obtained, and a similar trend to that of area variation was exhibited. However, the variation is greater at the 100% scale, compared to the area evaluation from Figure 6. The crack space formed at the 100% scale based on the TDPS method is significantly larger than the specimen volume since the volume of the test specimen is only 5.4×10^5 cm^3. The fact that the theoretical volume is greater than the actual volume of the test specimen does not mean that it is an error. The specimen is limited in size and the damage can only be confined and exhibited within the specimen. If the specimen boundary is expanded virtually, then the crack space has the potential to continue to expand. In this way, the results of the TDPS are well interpreted, demonstrating the ability to find potential crack spaces based on existing microcracks.

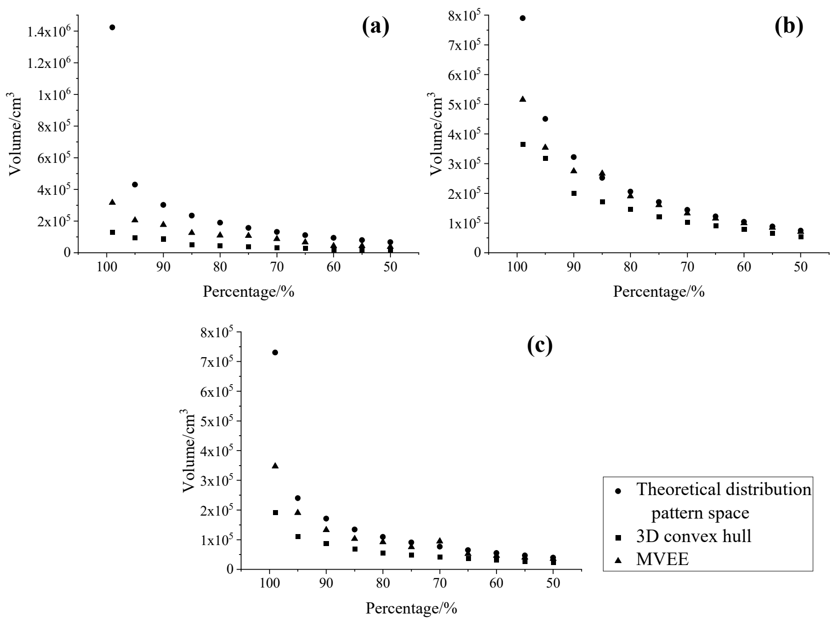

Figure 7. Volume evaluation of three methods. (**a**) Volume evaluation of Specimen S2. (**b**) Volume evaluation of Specimen S3. (**c**) Volume evaluation of Specimen S5.

Similar to the trend in area evolution, the results of the theoretical distribution pattern space and the MVEE method are gradually matched in volume values starting at 85%.

5.2. Evolution Pattern of Area and Volume

Although the results for the distribution and number of microcracks differed across specimens, the trends in the results for the three convex optimization methods are shared as the spatial scale of cracks decreases. In both area and volume, the results of all three methods show a trend of decreasing, exhibiting the potential of exponential functions. Therefore, the evolution pattern of area and volume can be assumed by Equation (15):

$$y = y_0 + Ae^{x/t} \tag{15}$$

where the parameter t is the scaling value of the horizontal coordinate, and the parameters y_0 and A are the translation value and scaling value of the vertical coordinates, respectively.

The fitting curves are shown in Figure 8. The goodness-of-fit R^2 values are listed in Table 1.

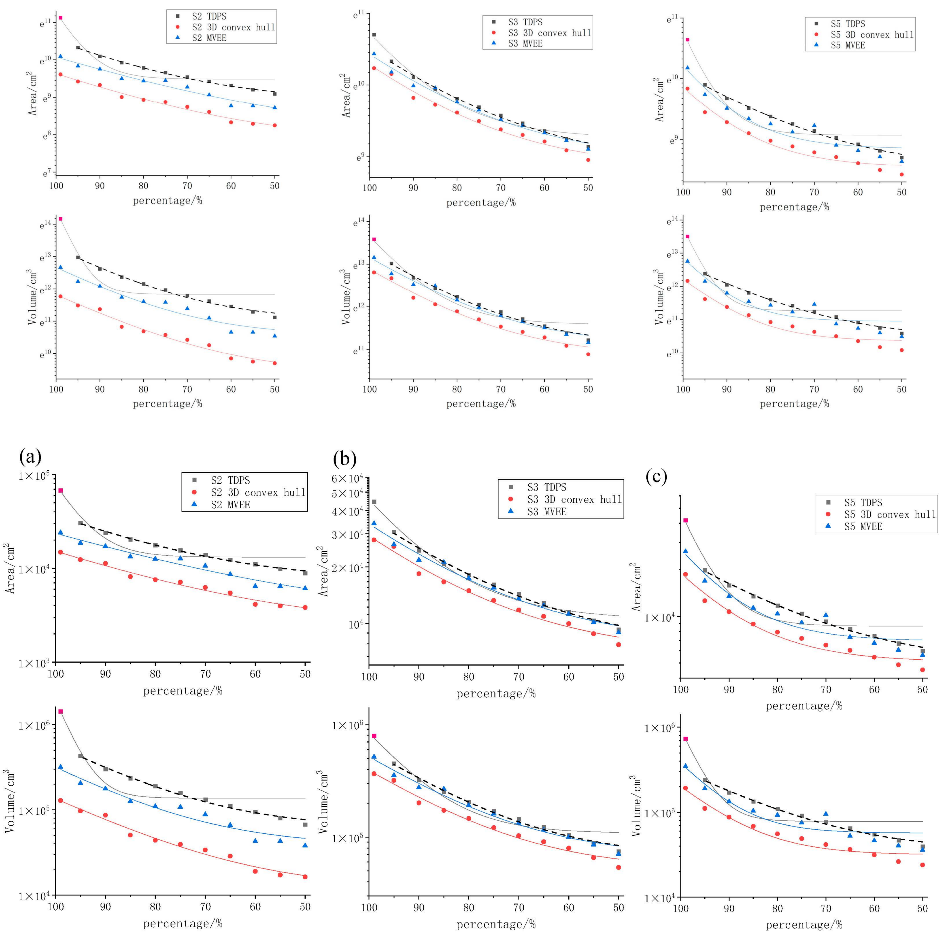

Figure 8. Fitting results of area and volume. (**a**) Fitting results of specimen S2. (**b**) Fitting results of specimen S3. (**c**) Fitting results of specimen S5. The black dashes are the fitting results after masking the maximum value.

Table 1. The goodness-of-fit R^2 of area and volume.

Specimen		S2			S3			S5	
Method	**TDPS**	**3DCH**	**MVEE**	**TDPS**	**3DCH**	**MVEE**	**TDPS**	**3DCH**	**MVEE**
Area	0.970	0.986	0.971	0.988	0.982	0.988	0.969	0.984	0.968
Volume	0.983	0.982	0.976	0.988	0.983	0.985	0.981	0.984	0.9670

Note: TDPS means the theoretical distribution pattern space, 3DCH means the 3D convex hull, and MVEE means the minimum volume enclosing ellipsoid.

The fitting results of both the area and volume were observed to comply with the exponential function, as shown in Figure 8. The mean values of the goodness-of-fit for the area and volume evolution were 0.978 and 0.981, respectively, indicating that Equation (15) can be used to interpret the evolution of area and volume.

5.3. Deviation Angles at Different Spatial Scales

In the assessment of crack space characteristics, area and volume were used to evaluate the size of the crack space. In addition, the directional characteristic is one of the significant parameters that must be evaluated. Based on the total microcrack distribution, the directions of the theoretical distribution pattern space are fixed, and do not vary with the spatial scales Therefore, they were set as the basis axes to analyze the deviation angles with the MVEE results.

It can be inferred from Section 3.3 that the theoretical distribution pattern space can be represented by a three-dimensional matrix, which is the covariance matrix $\boldsymbol{C}_{S^*}$. The direction of each axis of this crack space is represented by the eigenvector corresponding to the eigenvalue. In the same way, the ellipsoid ε from the MVEE method represented by a positive definite matrix $\boldsymbol{E}_m$ can be obtained, as well as the direction of its three axes. Thus, for the same spatial scale, the deviation angle of the MVEE ellipsoid can be obtained by calculating the angle between its principal axis and the principal axis of theoretical distribution pattern space. The deviation angles in each spatial scale were calculated and displayed in Figure 9.

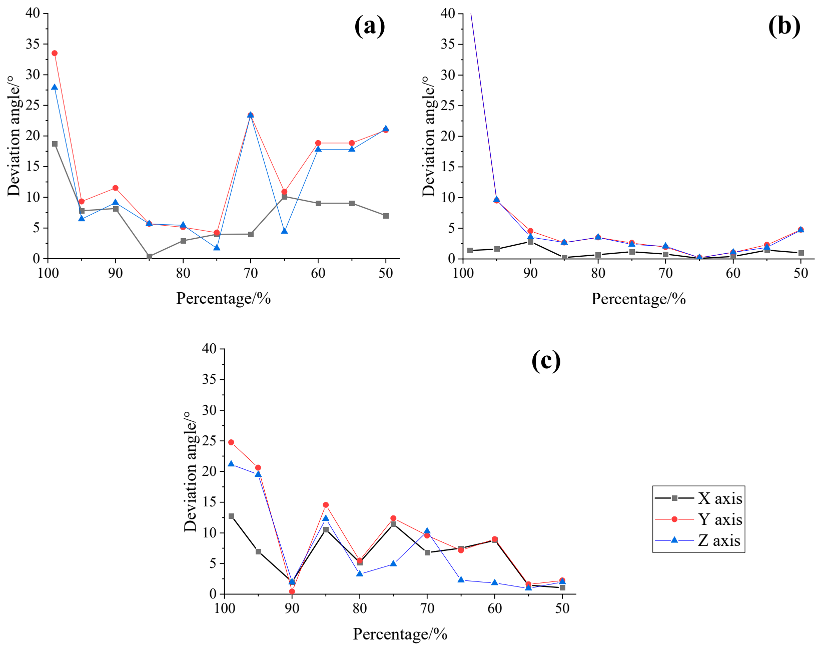

Figure 9. Results of deviation angle evolution. (**a**) Deviation angle evolution of Specimen S2. (**b**) Deviation angle evolution of Specimen S3. (**c**) Deviation angle evolution of Specimen S5.

It can be observed in Figure 9 that the *X*-axis deviation angles of three specimens were generally less than 10 degrees, with an average of 6.24 degrees, 1.01 degrees, and 6.17 degrees, respectively. They reached the relatively smallest values before the 85% scale, where the scale of the relative minimum value was reached at 90% in Figure 9c. After an increase, it began to show a decreasing trend again. Similar evolutionary trends were found on the other two axes. However, there was a tendency for the deviation angle to increase near 65%.

Considering the fact that microcracks are not evenly distributed within the specimen according to a theoretical distribution pattern, and a more dense distribution would be observed in the severely damaged zone [9,13,19], as the spatial scale decreases, there would be a situation where the crack space contains more densely distributed areas, with a lower share of other spatial regions [20,22]. Therefore, a reduction in spatial scale results in a loss of information about the crack space. In addition, the area and volume of the crack space are significantly underestimated, if the crack scale drops considerably. Therefore, a reliable crack space cannot be approached by continually reducing the spatial scale to approximate the minimum deviation angle. Summarizing the evolution of the evaluated values for the area, volume, and deviation angle, the appropriate spatial scale range for the crack space is proposed from 65% to 85%. This result is applicable only for these tests. The evaluation of different rock types requires further application to more rocks.

6. Conclusions

In this research, the spatial distribution of events monitored by rock acoustic emission is analyzed. The 3D convex hull algorithm and the MVEE algorithm were adopted to evaluate the single-cracked space formed by the theoretical distribution model, and the following three conclusions were obtained:

(1) AE events reflect the distribution of the real fracture, and it is considered that the microcracks expend with increasing stress in the stress direction. The theoretical distribution pattern space was proposed to characterize the crack space of a single-cracked fracture.

(2) The 3D convex hull, MVEE, and TDPS methods were applied to calculate the characteristics of the crack space. The area and volume results for all three methods demonstrated similar evolutionary behavior as the spatial scale decreased. The evolution pattern of area and volume was established. It was found that the 85% position is the scale on which the theoretical distribution and the MVEE values became closer to each other in three methods.

(3) The variations in the deviation angle between the MVEE and TDPS methods were compared. It was found that as the spatial interval decreases, there is a tendency for MVEE and TDPS methods to have smaller offset angles in the principal *X*-axis. Similar trends were found for the Y-axis and Z-axis results, but a tendency to increase was observed after 65%.

Consistent patterns of variation were obtained under conditions with different microcrack numbers and distributions, indicating that the present method is feasible. By analyzing the variation in area, volume characteristics, and offset angle through the spatial scale, 65% to 85% was selected as a reliable characterization interval for the crack space in sandstone.

Author Contributions: Conceptualization, X.H. (Xiaolin Hou); methodology, X.H. (Xiaolin Hou); data curation, Z.B., B.Z.; writing—original draft preparation, X.H. (Xiaolin Hou); writing—review and editing, C.W., H.Z., X.H. (Xiang He), X.S., T.W., X.L.; funding acquisition, X.H. (Xiaolin Hou), X.S. All authors have read and agreed to the published version of the manuscript.

Funding: This research was funded by the Special Fund of the Institute of Geophysics, China Earthquake Administration (grant number DQJB21K50), and Wuyi University introduced talents and started scientific research project (grant number YJ202202).

Institutional Review Board Statement: Not applicable.

Informed Consent Statement: Not applicable.

Data Availability Statement: The data used to support the findings of this study are available from the corresponding author upon request.

Acknowledgments: We thank the anonymous reviewers for their support to this study.

Conflicts of Interest: The authors declare no conflict of interest.

References

1. Hoek, E.; Martin, C.D. Fracture initiation and propagation in intact rock—A review. *J. Rock Mech. Geotech. Eng.* **2014**, *6*, 287–300. [CrossRef]
2. Anders, M.H.; Laubach, S.E.; Scholz, C.H. Microfractures: A review. *J. Struct. Geol.* **2014**, *69*, 377–394. [CrossRef]
3. Pan, B.; Qian, K.; Xie, H.; Asundi, A. Two-dimensional digital image correlation for in-plane displacement and strain measurement: A review. *Meas. Sci. Technol.* **2009**, *20*, 062001. [CrossRef]
4. Wang, C.; Lu, Z.; Liu, L.; Chuai, X.; Lu, H. Predicting points of the infrared precursor for limestone failure under uniaxial compression. *Int. J. Rock Mech. Min. Sci.* **2016**, *88*, 34–43. [CrossRef]
5. Xue, D.; Zhou, H.; Zhao, Y.; Zhang, L.; Deng, L.; Wang, X. Real-time SEM observation of mesoscale failures under thermal-mechanical coupling sequences in granite. *Int. J. Rock Mech. Min. Sci.* **2018**, *112*, 35–46. [CrossRef]
6. Wang, C.; Gao, A.; Shi, F.; Hou, X.; Ni, P.; Ba, D. Three-dimensional reconstruction and growth factor model for rock cracks under uniaxial cyclic loading/unloading by X-ray CT. *Geotech. Test J.* **2019**, *42*, 117–135. [CrossRef]
7. Grosse, C.U.; Finck, F. Quantitative evaluation of fracture processes in concrete using signal-based acoustic emission techniques. *Cement Concrete Compos.* **2006**, *28*, 330–336. [CrossRef]
8. Michlmayr, G.; Cohen, D.; Or, D. Sources and characteristics of acoustic emissions from mechanically stressed geologic granular media—A review. *Earth-Sci. Rev.* **2012**, *112*, 97–114. [CrossRef]
9. Wang, C.L. *Evolution, Monitoring and Predicting Models of Rockburst: Precursor Information for Rock Failure*; Springer Nature: Singapore, 2018.
10. Li, G.; Lu, R.; Ma, F.; Guo, J. Analysis of acoustic emission characteristics and failure mode of deep surrounding rock of Sanshandao Gold Mine. *Int. J. Environ. Res. Public Health* **2022**, *19*, 13351. [CrossRef]
11. Kourkoulis, S.K.; Pasiou, E.D.; Loukidis, A.; Stavrakas, I.; Triantis, D. Comparative assessment of criticality indices extracted from acoustic and electrical signals detected in marble specimens. *Infrastructures* **2022**, *7*, 15. [CrossRef]
12. Chen, D.; Li, N.; Wang, E. Temporal and spatial evolution of acoustic emission and waveform characteristics of specimens with different lithology. *J. Geophys. Eng.* **2018**, *15*, 1878–1888.
13. Zhang, S.; Wu, S.; Zhang, G.; Guo, P.; Chu, C. Three-dimensional evolution of damage in sandstone Brazilian discs by the concurrent use of active and passive ultrasonic techniques. *Acta Geotech.* **2020**, *15*, 393–408. [CrossRef]
14. Baud, P.; Schubnel, A.; Heap, M.; Rolland, A. Inelastic compaction in high-porosity limestone monitored using acoustic emissions. *J. Geophys. Res. Solid Earth* **2017**, *122*, 9989–10008. [CrossRef]
15. Katsaga, T.; Sherwood, E.G.; Collins, M.P.; Young, R.P. Acoustic emission imaging of shear failure in large reinforced concrete structures. *Int. J. Fract.* **2007**, *148*, 29–45. [CrossRef]
16. Liu, J.P.; Li, Y.H.; Xu, S.D.; Xu, S.; Jin, C.Y.; Liu, Z.S. Moment tensor analysis of acoustic emission for cracking mechanisms in rock with a pre-cut circular hole under uniaxial compression. *Eng. Fract. Mech.* **2015**, *135*, 206–218. [CrossRef]
17. Kourkoulis, S.K.; Pasiou, E.D.; Dakanali, I.; Stavrakas, I.; Triantis, D. Notched marble plates under tension: Detecting prefailure indicators and predicting entrance to the "critical stage". *Fatigue Frac. Eng. Mater. Struct.* **2018**, *41*, 776–786. [CrossRef]
18. Liu, X.; Zhang, H.; Wang, X.; Zhang, C.; Xie, H.; Yang, S.; Lu, W. Acoustic emission characteristics of graded loading intact and holey rock samples during the damage and failure process. *Appl. Sci.* **2019**, *9*, 1595. [CrossRef]
19. Lin, Q.; Wan, B.; Wang, Y.; Lu, Y.; Labuz, J.F. Unifying acoustic emission and digital imaging observations of quasi-brittle fracture. *Theor. Appl. Fract. Mech.* **2019**, *103*, 102301. [CrossRef]
20. López-Comino, J.A.; Cesca, S.; Heimann, S.; Grigoli, F.; Milkereit, C.; Dahm, T.; Zang, A. Characterization of hydraulic fractures growth during the Äspö hard rock laboratory experiment (Sweden). *Rock Mech. Rock Eng.* **2017**, *50*, 2985–3001. [CrossRef]
21. Goebel, T.H.W.; Becker, T.W.; Schorlemmer, D.; Stanchits, S.; Sammis, C.; Rybacki, E.; Dresen, G. Identifying fault heterogeneity through mapping spatial anomalies in acoustic emission statistics. *J. Geophys. Res. Solid Earth* **2012**, *117*, B03310. [CrossRef]
22. Yabe, Y.; Nakatani, M.; Naoi, M.; Philipp, J.; Janssen, C.; Watanabe, T.; Katsura, T.; Kawakata, H.; Georg, D.; Ogasawara, H. Nucleation process of an M2 earthquake in a deep gold mine in South Africa inferred from on-fault foreshock activity. *J. Geophys. Res. Solid Earth* **2015**, *120*, 5574–5594. [CrossRef]
23. Hohl, A.; Griffith, A.D.; Eppes, M.C.; Delmelle, E. Computationally enabled 4D visualizations facilitate the detection of rock fracture patterns from acoustic emissions. *Rock Mech. Rock Eng.* **2018**, *51*, 2733–2746. [CrossRef]
24. Wang, C.; Hou, X.; Liu, Y. Three-dimensional crack recognition by unsupervised machine learning. *Rock Mech. Rock Eng.* **2021**, *54*, 893–903. [CrossRef]
25. Wang, C.; Liu, Y.; Hou, X.; Elmo, D. Investigation of the spatial distribution pattern of 3D microcracks in single-cracked breakage. *Int. J. Rock Mech. Min.* **2022**, *154*, 105126. [CrossRef]
26. Mayerhofer, M.J.; Lolon, E.; Warpinski, N.R.; Cipolla, C.L.; Walser, D.W.; Rightmire, C.M. What is stimulated reservoir volume? *SPE Prod. Oper.* **2010**, *25*, 89–98. [CrossRef]
27. Li, L.; Tan, J.; Wood, D.A.; Zhao, Z.; Becker, D.; Lyu, Q.; Shu, B.; Chen, H. A review of the current status of induced seismicity monitoring for hydraulic fracturing in unconventional tight oil and gas reservoirs. *Fuel* **2019**, *242*, 195–210. [CrossRef]
28. Schwartzkopff, A.K.; Melkoumian, N.S.; Xu, C. Breakdown pressure and propagation surface of a hydraulically pressurized circular notch within a rock material. *Rock Mech. Rock Eng.* **2020**, *54*, 191–218. [CrossRef]

29. Lin, A.; Ma, J. Stimulated-rock characteristics and behavior in multistage hydraulic-fracturing treatment. *SPE J.* **2015**, *20*, 784–789. [CrossRef]
30. Shao, Y.; Huang, X.; Xing, Y. An integrated study on the sensitivity and uncertainty associated with the evaluation of stimulated reservoir volume (SRV). *J. Pet. Sci. Eng.* **2017**, *159*, 903–914. [CrossRef]
31. Cui, G.; Tan, Y.; Chen, T.; Feng, X.T.; Elsworth, D.; Pan, Z.; Wang, C. Multidomain two-phase flow model to study the impacts of hydraulic fracturing on shale gas production. *Energy Fuels* **2020**, *34*, 4273–4288. [CrossRef]
32. Hubbert, M.K.; Willis, D.G. Mechanics of hydraulic fracturing. *Mem. Am. Assoc. Pet. Geol.* **1972**, *18*, 153–163. [CrossRef]
33. Healy, D.; Jones, R.R.; Holdsworth, R.E. Three-dimensional brittle shear fracturing by tensile crack interaction. *Nature* **2006**, *439*, 64–67. [CrossRef]
34. Meredith, P.G.; Atkinson, B.K. Stress corrosion and acoustic emission during tensile crack propagation in Whin Sill dolerite and other basic rocks. *Geophys. J. Int.* **1983**, *75*, 1–21. [CrossRef]
35. Dalguer, L.A.; Irikura, K.; Riera, J.D. Simulation of tensile crack generation by three-dimensional dynamic shear rupture propagation during an earthquake. *J. Geophys. Res. Solid Earth* **2003**, *108*. [CrossRef]
36. Freund, L.B. The mechanics of dynamic shear crack propagation. *J. Geophys. Res. Solid Earth* **1979**, *84*, 2199–2209. [CrossRef]
37. Ohno, K.; Ohtsu, M. Crack classification in concrete based on acoustic emission. *Constr. Build. Mater.* **2010**, *24*, 2339–2346. [CrossRef]
38. Li, Y.H.; Liu, J.P.; Zhao, X.D.; Yang, Y.J. Experimental studies of the change of spatial correlation length of acoustic emission events during rock fracture process. *Int. J. Rock Mech. Min.* **2010**, *47*, 1254–1262. [CrossRef]
39. Barber, C.B.; Dobkin, D.P.; Huhdanpaa, H. The quickhull algorithm for convex hulls. *ACM Trans. Math. Softw.* **1996**, *22*, 469–483. [CrossRef]
40. Kumar, P.; Yildirim, E.A. Minimum-volume enclosing ellipsoids and core sets. *J. Optim. Theory Appl.* **2005**, *126*, 1–21. [CrossRef]
41. Khachiyan, L.G. Rounding of polytopes in the real number model of computation. *Math. Oper. Res.* **1996**, *21*, 307–320. [CrossRef]
42. Moradian, Z.; Einstein, H.H.; Ballivy, G. Detection of cracking levels in brittle rocks by parametric analysis of the acoustic emission signals. *Rock Mech. Rock Eng.* **2016**, *49*, 785–800. [CrossRef]
43. Zhou, X.P.; Zhang, J.Z.; Qian, Q.H.; Niu, Y. Experimental investigation of progressive cracking processes in granite under uniaxial loading using digital imaging and AE techniques. *J. Struct. Geol.* **2019**, *126*, 129–145. [CrossRef]
44. Wong, L.N.Y.; Xiong, Q.Q. A Method for multiscale interpretation of fracture processes in carrara marble specimen containing a single flaw under uniaxial compression. *J. Geophys. Res. Solid Earth* **2018**, *123*, 6459–6490. [CrossRef]
45. Moore, D.E.; Lockner, D.A. The role of microcracking in shear-fracture propagation in granite. *J. Struct. Geol.* **1995**, *17*, 95–114. [CrossRef]